HHS Public Access

Author manuscript

NMR Biomed. Author manuscript; available in PMC 2017 October 01.

Published in final edited form as:

NMR Biomed. 2016 October ; 29(10): 1350–1363. doi:10.1002/nbm.3577.

Pulsed and oscillating gradient MRI for assessment of cell size and Extracellular space (POMACE) in mouse gliomas

Olivier Reynaud[1,2,*], **Kerryanne Veronica Winters**[1,2], **Dung Minh Hoang**[1,2], **Youssef Zaim Wadghiri**[1,2], **Dmitry S. Novikov**[1,2], and **Sungheon Gene Kim**[1,2]

[1]Center for Advanced Imaging Innovation and Research (CAI^{2}R), New York, NY USA

[2]Bernard and Irene Schwartz Center for Biomedical Imaging, Department of Radiology, New York University School of Medicine, New York, NY USA

Abstract

Solid tumor microstructure is related to aggressiveness of tumor, interstitial pressure and drug delivery pathways that are closely associated with treatment response, metastatic spread and prognosis. In this study, we introduce a novel diffusion MRI data analysis framework, Pulsed and Oscillating gradient MRI for Assessment of Cell size and Extracellular space (POMACE), and demonstrate its feasibility in a mouse tumor model.

In vivo and ex vivo POMACE experiments were performed on mice bearing the GL261 murine glioma model (n=8). Since the complete diffusion time-dependence is in general non-analytical, the tumor microstructure was modeled in an appropriate time/frequency regime by impermeable spheres (radius R_{cell}, intracellular diffusivity D_{ics}) surrounded by extracellular space (approximated by constant apparent diffusivity D_{ecs} in volume fraction ECS). POMACE parametric maps (ECS, R_{cell}, D_{ics}, D_{ecs}) were compared with conventional diffusion weighted imaging metrics, electron microscopy (EM), alternative ECS determination based on effective medium theory (EMT), and optical microscopy performed on the same samples.

It was shown that D_{ecs} can be approximated by its long-time tortuosity limit in the range [1/(88 Hz) - 31 ms]. ECS estimations (44±7% in vivo and 54±11% ex vivo) were in agreement with EMT-based ECS and literature on brain gliomas. Ex vivo, ECS maps correlated well with optical microscopy. Cell sizes (R_{cell}=4.8±1.3 in vivo and 4.3±1.4 μm ex vivo) were consistent with EM measurements (4.7±1.8 μm).

In conclusion, R_{cell} and ECS can be quantified and mapped in vivo and ex vivo in brain tumors using the proposed POMACE method. Our experimental results support that POMACE provides a way to interpret the frequency- or time-dependence of the diffusion coefficient in tumors in terms of objective biophysical parameters of neuronal tissue, which can be used for non-invasive monitoring of preclinical cancer studies and treatment efficacy.

[*]Address all correspondence to: Olivier Reynaud, PhD, Laboratoire d'Imagerie Fonctionnelle et Metabolique (LIFMET), Ecole Polytechnique Federale de Lausanne (EPFL), Station 6, CH-1015 Lausanne, Switzerland oli.reynaud@gmail.com; Tel: +041-216-93-7671.

Keywords

Extracellular Space; Diffusion time-dependence; Oscillating Gradients Spin Echo; Glioma; Restrictions; POMACE

INTRODUCTION

Solid tumor microstructure is related to aggressiveness of tumor, interstitial pressure and drug delivery pathways that are closely associated with treatment response, metastatic spread and prognosis (1–4). In particular, the extracellular space volume fraction (ECS) has been recognized as a strong biomarker for tumor response and treatment efficacy (1). Similarly, differences in cell size can reflect various cancer types (5) or apoptosis following treatment (6). However, very few methods provide an accurate estimation of the ECS (7) or dimensions of the relevant cellular structures at the microscopic scale. In addition, many of these approaches involve radioactive extracellular tracers, optical imaging or iontophoresis (7–9), which are invasive and cannot be translated to clinical cases.

Diffusion MRI has been recognized as a potentially powerful non-invasive tool to probe tumor microenvironment (10–12), but the apparent diffusion coefficient (ADC) remains only a qualitative marker for cellularity (11,13). Since a diffusion measurement at a fixed diffusion time is affected by multiple factors, such as cell size, cell density, composition of the extracellular matrix, and compartmental diffusivities, recent work have focused on temporal diffusion spectroscopy (i.e. time-dependent diffusion) combined with tissue modeling (14,15) to gain insight on the ECS and cell size. This approach was successful in identifying cortical areas of various cellularity ex vivo (16), and recognizing apoptotic from healthy cells in vitro (17). However, to date, there has not been any report on characterizing the tumor cell size and ECS volume fraction in vivo and ex vivo using temporal diffusion spectroscopy.

The time-dependence of the diffusion coefficient indicates the presence of barriers that restrict the otherwise free diffusion. The relationship between diffusion time dependence and the size of the restricting compartment has been studied for the brain (14,18–20) and muscle tissues (21–24). The characteristic time for restrictive effects is $\tau_R \sim L^2/D$, where L is a typical distance water molecules travel to encounter the barriers and D is the diffusivity of the bulk fluid. For cancer cells, with radius ~ 4 μm and D ~ 1.5 μm^2/ms, the effects of restriction is expected to be observed when diffusion time is about $\tau_R \sim 10$ ms. This means that diffusion times ranging from a substantially shorter than 10 ms to a substantially longer than 10 ms are required to study restricted diffusion in cancer cells. It is not trivial to achieve this particular range of diffusion times using either pulsed gradient spin echo (PGSE) or oscillating gradient spin echo (OGSE) diffusion experiment alone on conventional preclinical hardware. Hence, we consider a combination of both sequences in this study.

PGSE and OGSE-based diffusion inside simple structures, such as impermeable cylinders and spheres, have been investigated earlier (14,25). Recent studies have used these geometrical models to assess the degree of vasculature of various tumors (26), or identify cancer cells of different sizes in vitro (27) or in vivo following chemotherapeutic treatment

(25). However, the functional dependence of the extracellular diffusivity at low frequency is non-analytic due to the disordered arrangement of restrictions, and is thereby fundamentally distinct from that in regular geometries (24). Simple Gaussian diffusion models are in general inadequate for quantifying tissue properties whenever the measurements are mostly sensitive to low frequencies or long times (19,20). In addition, even in the simplest models, the large number of parameters required to model the tumor microenvironment affects the fits robustness, making these studies very sensitive to a priori assumptions or knowledge on the underlying microstructure, which can be very disordered and/or spatially heterogeneous in the case of aggressive tumors (28–30).

In this study, we introduced a novel data acquisition and analysis framework referred to as Pulsed and Oscillating gradient MRI for Assessment of Cell size and Extracellular space (POMACE) and investigated the feasibility of using POMACE to estimate the extracellular space volume fraction and cell size of brain tumors in vivo and ex vivo. ECS measurements from in vivo and ex vivo POMACE experiments were compared with an alternate ECS estimation method based on effective medium theory (EMT). In addition, optical microscopy was performed on the same samples, and Electron Microscopy (EM) was performed for the assessment of cell radius on the same cell line. The scope of our study was limited to solid tumor tissue and it did not include normal brain tissue that requires different geometrical considerations and experimental conditions.

THEORY - POMACE

1. Diffusion model of tumor microstructure

In the POMACE framework, we assume the simplest case of a tumor microstructural model in which the diffusion MR signal S can be expressed, in absence of exchange, as the sum of signals from intra- and extra-cellular spaces, S_{ics} and S_{ecs}, respectively;

$$S=(1-ECS)*S_{ics}+ECS*S_{ecs} \quad [1]$$

In general, tissue complexity manifests itself in the non-Gaussian diffusion (31,32), characterized by the presence of the higher-order terms in the cumulant expansion of MR signal S (33),

$$\ln(S)=-bD+(K/6)\cdot(bD)^2+\cdots \quad [2]$$

where D and K represent the diffusion and kurtosis coefficients (34), and by the time-dependence of all the cumulants: $D(\tau)$, $K(\tau)$, … (35). The requirement to use short diffusion times in this study limits the range of practically achievable b-values to under 1 ms/μm^2, even with OGSE sequences and on preclinical scanners with strong gradient inserts compared to clinical scanners. For such low b-values, second and higher order terms of the cumulant expansion are negligible (33). As a result, for each diffusion time τ (or

equivalently, oscillation frequency $\omega \sim 1/\tau$), the total diffusion MR signal can be adequately described by a single diffusion coefficient equal to the weighted average of both diffusion coefficients:

$$D(\tau)=-\lim_{b\to 0}\frac{\partial}{\partial b}\ln S(\tau)=(1-ECS)\cdot D_{ics}(\tau)+ECS\cdot D_{ecs}(\tau). \quad [3]$$

The lowest order approximation of this cumulant expansion (also known as DTI regime) (14,25,36) was previously shown valid in this range of *b*-values and for this tumor model (37).

Furthermore, the cell membrane is considered impermeable in the range of diffusion times used in this study (τ <31 ms). It allows one to assume no exchange of the water molecules between the intracellular and extracellular spaces, cf. Eq. [1]. This hypothesis is supported by previous studies of intracellular water residence time that reported 400 ms for human breast tumors (38), 317±17 ms for fixed human myelogenous leukemia K562 cells (39), 344±1.3 ms in viable human brain tumor (40) and 146–714 ms for tumor cells undergoing apoptosis (41). The range of relatively short diffusion times probed in this experiment is selected intentionally in order to neglect the influence of membrane permeability on time-dependent diffusion.

2. Intracellular compartment

Here we represent cancer cells by identical spheres of radius R_{cell}, and free intracellular diffusivity D_{ics}. In the DTI regime, the signal attenuation inside impermeable spheres due to diffusion-encoding gradients $S_{ics} = \exp(-b \cdot D_{app}(R_{cell}, D_{ics}))$ was derived for cosinusoidal OGSE (14) and PGSE (25), and successfully applied to cellular and nuclear (42) as well as axonal size estimation (43). For an integer number of oscillations:

$$D_{OGSE}(\omega)=2D_{ics}(\omega\tau_R)^2\sum_n\frac{1}{(\mu_n^2-2)}\left\{\frac{1}{\mu_n^4+(\omega\tau_R)^2}+\frac{2\mu_n^2\frac{\tau_R}{\delta}}{\left(\mu_n^4+(\omega\tau_R)^2\right)^2}\left[\exp\left(-\mu_n^2\frac{\delta}{\tau_R}\right)-1+\exp\left(-\mu_n^2\frac{\Delta}{\tau_R}\right)\left[1-\cosh\left(\mu_n^2\frac{\delta}{\tau_R}\right)\right]\right]\right\}$$

[4]

where δ is the gradient duration, Δ the inter-gradient duration and $\tau_R=R_{cell}^2/D_{ics}$ represents the characteristic diffusion time for a cell. For a spherical geometry, μ_n is the nth root of the function $\partial j_1(\mu)/\partial\mu$, where $j_1(\mu) = (\sin(\mu) - \mu\cdot\cos(\mu))/\mu^2$ is the spherical Bessel function of the first kind, which is equivalent to the formulation in (14). For OGSE, the diffusion time can be approximated by $\pi/2\omega$.

Using the same formalism, the formula for spherical attenuation with PGSE is given by:

$$D_{PGSE}(\tau=\Delta)=4\frac{R^2}{(\Delta-\delta/3)}\left(\frac{\tau_R}{\delta}\right)^2\sum_n\frac{1}{\mu_n^6(\mu_n^2-2)}\left\{\mu_n^2\frac{\delta}{\tau_R}-1+\exp\left(-\mu_n^2\frac{\delta}{\tau_R}\right)+\exp\left(-\mu_n^2\frac{\Delta}{\tau_R}\right)\left[1-\cosh\left(\mu_n^2\frac{\delta}{\tau_R}\right)\right]\right\}$$

[5]

originally derived by Murday and Cotts (25). For PGSE, the inter-gradient duration Δ is identified as the diffusion time τ.

Eq. [4] scales as $D_{OGSE}(\omega) \sim \omega^2$ in the very long time limit ($\omega \rightarrow 0$). In the short time limit ($\omega \rightarrow \infty$), it behaves as $\omega^{-1/2}$ in agreement with (44,45). Such trend of time-dependent intracellular diffusivity is illustrated in Fig. 1A. It can be noted that the frequency range of the long and short time regimes depends on the particular cell size and intracellular diffusivity. For instance, Fig. 1A demonstrates that OGSE diffusion data with R_{cell} = 1 μm are in the long time regime for f_{OGSE} = [100–200] Hz, whereas those with R_{cell} = 4 μm and beyond are in the short time regime.

3. Extracellular compartment (general case)

The time-dependence of diffusion in the ECS depends on the multiple pathways available to water molecules, which in turn depends on the specific geometrical arrangement and packing disorder of cells (24). How each of these parameters impact the ECS diffusion is unknown. Depending on the range of diffusion times/frequencies probed in the study, different assumptions can be made to properly model the tumor microenvironment. In addition, ECS short/intermediate/long time regimes do not necessarily match those defined for the intracellular compartment.

3.1. Short time regime ($\tau \sim \omega^{-1} \ll \tau_R$)—The Mitra (or short time) limit (44,46) characterizes the time/frequency regime where the mean displacement of water molecules labeled using magnetic field gradients is negligible compared to the distance between restrictions imposed by the micro-environment (i.e. cell membranes). The universal form of the OGSE diffusion coefficient in this regime, valid for both intra- and extracellular spaces, is characterized by a linear relationship with $\omega^{-1/2}$ (45). For a cosinusoidal waveform, the analytical expression of the OGSE-measured diffusion coefficient $D(\omega)$ is fully described by the medium free diffusivity D_0 and the surface-to-volume ratio of the restrictions S/V (44,45), such that:

$$D(\omega)=D_0(1-c(N)\cdot c_d\cdot S/V\cdot\sqrt{D_0/\omega}),\quad c_d=1/3\sqrt{2} \qquad [6]$$

for isotropic diffusion in d=3 dimensions relevant for glioma in the gray matter. Here ω is the oscillation frequency ($\omega = 2\pi f_{OGSE}$), and $c(N)$ is a correction factor monotonically decreasing with the number of oscillations N (47),

$c(N)=\left\{4\pi N * C(2\sqrt{N})+3 * S(2\sqrt{N})\right\}/(2\pi N)$ (where $C(x)$ and $S(x)$ are the Fresnel functions) such that $c(\infty) = 1$.

3.2. Long time regime ($\tau \sim \omega^{-1} \gg \tau_R$)—Based on the micro-structural organization, it is possible to grasp a functional form of the ECS diffusion in the very long time limit (Fig. 1B, left column). For OGSE, since short-range disorder is more likely to characterize relatively dilute structures such as cancer cells lacking any particular long-range order, the diffusion coefficient can be expressed as $D_{ecs}(\omega)=D_{ecs}^{\infty}+\mathrm{const}\cdot\omega^{d/2}$ in d dimensions (see Fig. 2A in (24)). For PGSE, it was previously shown (24,48) that, in 3 dimensions, the extracellular $D(\tau)$ increases in the long time limit ($\tau \rightarrow \infty$) with the inverse of time, as in:

$$D(\tau)=D^{\infty}+A/\tau+O(\tau^{-3/2}), \quad [7]$$

where A is a structure-dependent positive parameter independent of diffusion time τ. Based on Eq. [5], the functional form of Eq. [7] is also valid at long times for the intracellular compartment, with $D^{\infty} = 0$.

3.3. Intermediate time regime—While the molecular restrictions inside impermeable spherical boundaries can be quantified for any oscillation frequency (14), there is to date no analytical solution for the diffusion in the ECS at intermediate times/frequencies (Fig. 1B, second column). As a result, modeling the diffusion coefficient outside the very short/long time regime is not trivial. Depending on the oscillation frequency range and cellular size, the time-dependence of the overall diffusion coefficient can be dominated by each of the two compartments (intra- or extracellular). Boundaries between short and intermediate (ω_1), and between intermediate and long time regimes (ω_2) are related to the free/restricted diffusivities $D_{0,ecs}/D_{ecs}^{\infty}$ and characteristic packing correlation length l_c and cell size R_{cell} ($l_c \gtrsim R_{cell}$), as in $\omega_1 = D_{0,ecs}/R_{cell}$ and $\omega_2=D_{ecs}^{\infty}/l_c$, such that $\omega_1 \gtrsim \omega_2$, Fig. 1B. The extent of this regime depends therefore on the particular packing arrangement of the medium (l_c vs. R_{cell}).

4. Extracellular compartment (approximation)

The PGSE/OGSE time/frequency range sensitizes MR acquisitions to specific diffusion lengths (i.e. cellular sizes). While diffusion in small structures is highly restricted (Fig. 1A, $R_{cell} \geq 1$ μm) in the range [50–225] Hz accessible with our scanner, this domain is well adapted to capture major time-dependent changes inside larger cancer cells (Fig. 1A, $R_{cell} =$ 4 μm). Outside the ECS short time regime (i.e., $f_{OGSE} <$ 88 Hz (37)), D_{ecs} cannot be described analytically. However, relatively small change in D_{ecs}, compared to that in D_{ics}, is expected for diffusion times longer than the characteristic time scale τ_R, as depicted by the double arrow in Fig. 1B. A similar situation was highlighted by a recent simulation study in one dimension (Fig. 1C in (24)). In 3 dimensions, due to the many pathways accessible to water molecules around “compact” restrictions such as spherical cells, and due to relatively low cellular packing in brain gliomas ($ECS \sim$ 40–50 %, see (1)), we expect an overall small difference between D_{ecs}^{∞} and its free value $D_{0,ecs}$. (The EMT estimate, discussed around Eq

[9] below, yields $D_{ecs}^{\infty} \approx \sqrt{0.5} D_{0,ecs}$ for ECS occupying 50% of the volume, suggesting the overall drop from $D_{0,ecs}$ to D_{ecs}^{∞} of about 30%.) These observations suggest that the overall diffusion coefficient time-dependence, in the range [1/(88 Hz) - 31 ms], mainly originates from the intracellular compartment. Hence, we hypothesized that the diffusion in the ECS, D_{ecs}, can be practically viewed as time-/frequency-*independent* outside the short time regime (i.e., $f_{OGSE} < 88$ Hz) and thereby can be approximated by its tortuosity limit $D_{ecs} \cong D_{ecs}^{\infty}$. The diffusion-weighted extracellular MR signal is then given by $S_{ecs} = \exp(-bD_{ecs})$. As explained earlier, this assumption is not trivial and its validity will be investigated further with our experimental data in this study. While D_{ecs}^{∞} provides an inferior bound for D_{ecs}, a superior bound can be derived from the Mitra regime, as Eq. [6] still holds for $f_{OGSE} = 88$ Hz (26).

5. POMACE parameter estimation

The proposed POMACE model has four parameters (ECS, R_{cell}, D_{ics}, *and* D_{ecs}) to characterize tumor microstructure. Note that this model is based on the geometrical considerations relevant to tumor cells, not normal brain tissue, as described above. Among the four parameters, we can utilize an additional relationship between ECS and D_{ics} in the short time regime. For OGSE, it was previously shown that the Mitra regime is reached in the GL261 mouse glioma model for oscillation frequencies f_{OGSE} above 88 Hz, as illustrated in supplementary Figure S1: above that threshold, the S/V estimation based on Eq. [6] is independent of temperature as it reflects purely geometric restrictions (37). Since $D(\omega)$ varies linearly with $\omega^{-1/2}$ in each compartment (intra-/extracellular) in this short time regime, the functional form given by Eq. [6] remains valid for the weighted average D defined in Eq. [3] and, in particular, for its asymptotic limit D_0 at infinite frequencies. Then, our system of equations simplifies to:

$$D_0 = (1 - ECS) \cdot D_{ics} + ECS \cdot D_{0,ecs}, \quad [8a]$$

$$D(\tau) = (1 - ECS) \cdot D_{PGSE}(\tau, R_{cell}, D_{ics}) + ECS \cdot D_{ecs}, \text{ and} \quad [8b]$$

$$D(\omega) = (1 - ECS) \cdot D_{OGSE}(\omega, R_{cell}, D_{ics}) + ECS \cdot D_{ecs}. \quad [8c]$$

The estimation of the POMACE model parameters is performed in two steps: (1) estimate D_0 and S/V from the OGSE data in the short diffusion time via Eq. [6]; (2) estimate the four model parameters (ECS, R_{cell}, D_{ics}, *and* D_{ecs}) by fitting Eq. [8b/c] to the PGSE and low-frequency OGSE data with Eq. [8a] as a constraint for ECS and D_{ics}, using a fixed $D_{0,ecs}$ (as described in Methods section).

6. Alternative ECS estimation via the Effective Medium Theory

Using the Effective Medium Theory (EMT), the long time limit of the diffusion coefficient D^{∞} was derived for packed erythrocytes surrounded by extracellular space (49). In the approximation of impermeable membranes, the link between D^{∞} and ECS (equation [2] from ref. (49)) becomes independent of the sphere radius R_{cell} and simplifies to:

$$D^{\infty}=ECS\cdot D_{ecs}^{\infty}=ECS\cdot(ECS^{1/2}\cdot D_{0,ecs})=ECS^{3/2}\cdot D_{0,ecs}, \quad [9]$$

where $D_{0,ecs}$ is the free diffusivity in the ECS in the absence of restrictions. The EMT value D_{ecs}^{∞} and the EMT-based ECS estimates (via Eqs. [7] and [9]) will be compared to the D_{ecs} and ECS fit estimates based on the system of equations [8], under the same hypotheses of impermeable membranes and free extracellular diffusivity values (2.7/1.94 μm^2/ms in vivo/ex vivo). Compared to POMACE, the EMT framework is expected to provide a more robust ECS estimation, due to the small number of parameters to fit, at the expense of cell size information.

METHODS

Noise propagation study

A noise propagation study was performed to assess the uncertainty in POMACE model parameter estimation. DWI data were generated based on Eqs. [3–6], and Gaussian noise was added to the diffusion coefficient estimation (SNR=25/50/100, two data-points per time/frequency, n=600). The influence of initial guess was minimized by starting from the true parameter set used to generate the data. Estimation of the model parameters from the low frequency OGSE and PGSE noisy data was performed with and without the additional constraint in Eq. [8a].

Animal model

Female C57BL/6 mice (n=8, 6–8 weeks) were used to generate murine orthotopic glioma models. GL261 cells (n=10^6), suspended in 5 μL phosphate buffered saline (PBS), were injected into the subcortex (2.5 mm depth) using a Hamilton syringe (1 μL/min) (36). All mice were treated in strict accordance with the National Institutes of Health Guide for the Care and Use of Laboratory Animals, and the experimental procedures were performed in accordance with the Institutional Animal Care and Use Committee at the New York University School of Medicine.

In vivo imaging protocol

MRI experiments were conducted using a 7T Biospec micro-MRI system (Bruker Biospin MRI, Ettlingen, Germany) equipped with a Bruker BGA-9S gradient coil (750 mT/m gradient strength). All mice were scanned once between 2 and 4 weeks after tumor implantation. Animals were imaged using an in-house built quadrature Litz coil. Mice were anesthetized and positioned inside a custom-built mouse mold (50). A bite bar and head strap were used to ensure minimal motion during the scan. Respiration and temperature were closely monitored and kept stable (60±10 bpm and T=35±1°C) throughout the entire MR

session. General anesthesia was maintained using 1.5% isoflurane in air. In vivo DWI consisted of OGSE and PGSE measurements, probing four diffusion times Δ = 6/9/16/31 ms for PGSE (δ=2/3 ms), and ten oscillation frequencies in the range [65–225] Hz for the fast-ramp cosinusoidal OGSE (51) (total number of oscillations $2 \leq N \leq 10$). Previous studies (37) revealed mono-exponential signal behavior, i.e., negligible Intra-Voxel Incoherent Motion effect, and isotropic diffusion in the tumor for $b<0.4$ ms/μm^2 (=400 s/mm^2). Hence, diffusion-weighting gradients were applied in only one direction (1, 1, 1), using b=[0, 0.2, 0.4] ms/μm^2. Scans were performed with a single slice positioned at the tumor center. The Spin-Echo EPI scan parameters were: TR/TE = 3000/70 ms, Bandwidth 300 kHz, 1 readout segment, number of averages NA=20, number of repetitions NR=2, pixel resolution 0.25x0.25x1.5 mm, matrix 80x80, acquisition time 6 min per frequency/diffusion time, and total scan time 84 min. Diffusion times and oscillation frequencies were randomly sampled during the session. The whole series was repeated twice to monitor any changes due to temperature/motion. Representative images for OGSE EPI and corresponding diffusion coefficient maps (in vivo and ex vivo) can be found online (supplementary materials Fig. S2).

Ex vivo sample preparation

Mice were sacrificed following the in vivo imaging. Following transcardiac perfusion (PBS + 4% PFA), the brains were extracted, preserved in multiple sucrose solutions and kept in optimal-compound temperature media using the protocol described in (36). After embedding, 5 μm and 100 μm thickness sections were cut for immunohistochemical (IHC) staining of GLUT1/hematoxylin and ex vivo MR imaging, respectively.

Prior to ex vivo imaging, brain sections were rehydrated in PBS for two hours and sealed between two coverslips (48). Provided proper sealing, previous ex vivo experiments using this particular setup and diffusion imaging protocol showed minimal tissue dehydration and MR distortion, very good stability of the samples during overnight scans and a good image reproducibility, both at room temperature and at 37°C (37).

Ex vivo MR coil and DWI protocol

A dual-coverslip histology coil was used for ex vivo scans (52). Each sample placed in the histology coil (n=8) was carefully positioned in the horizontal plane and kept at room temperature. The diffusion-weighting direction was set in the horizontal plane to minimize any coverslip-induced restriction effect. The ex vivo MR protocol was adjusted as follows: NA=40, NR=6, and total acquisition time 11 hours. Other than that, the scan protocol for ex vivo DWI scan was same as the in vivo scan as our pilot study found that the diffusivity changes between in vivo and ex vivo scans were well within the expected 30% change due to temperature decreased from 37 °C to 20 °C.

Local temperature was monitored using (i) a thermocouple placed next to the histocoil and (ii) repetitions of the diffusion protocol through the entire session, such that any drift in temperature would be detected via temporal changes of the measured diffusion coefficient. No drift was observed during ex vivo imaging, neither at scan nor session level. The imaging slice thickness (1.5 mm) was chosen larger than the sample thickness (0.1 mm) so that small

drifts perpendicular to the imaging plane would not impact MR measurements through the imaging session. In addition, EPI trajectories were re-acquired for each scan and the water frequency adjusted every hour to compensate for potential slow drifts of the water frequency. No tissue deformation was detected during the imaging session. B-values could not be adjusted (i.e. increased) for the decreased diffusivities expected during ex vivo scans at room temperature due to hardware limitations, resulting in a two-fold SNR decrease compared to in vivo scans.

Optical Microscopy

The same ex vivo samples used for MRI were immersed in PBS, mounted between two coverslips (n=8) and imaged with optical microscopy (Zeiss LSM510 confocal microscope), at x10 magnification, without staining. Depending on sample size, 18 to 90 images were acquired sequentially within a rectangular grid. High resolution images were stitched together using the “Stitching” Fiji plugin for ImageJ (53).

Electron Microscopy

One additional animal was sacrificed at Day 14 after tumor implantation. Its brain was perfused with PBS (30s) followed by a fixative solution (2% PFA, 2.5% Glutaraldehyde, 0.1M sucrose) (one hour). After dissection of the brain, the tumor was extracted for further fixation (two hours, same fixative) and kept at 4 °C overnight. The sample was then rinsed in a series of PB (Na2HPO4+NaH2PO4) solutions (0.1 then 0.2M), fixed in osmium tetroxide, rinsed in double distilled water, dehydrated in a series of alcohol solutions (30 to 95%), and rinsed in ethanol then propylene oxide (PO). It was then left in a PO:EMbed812 solution (proportions: 1:1 for one hour followed by 1:2 overnight at 4°C). The next day, the sample was rinsed twice in a mixture of EMbed812 and anhydrides (two times two hours in fresh solution), then embedded at 65°C. After 4 days at 65°C, the sample was trimmed for EM gridding.

EM was performed on thin sections (70 nm) at x2560 magnification (0.013 μm in plane resolution). Sixty eight images were acquired within a grid covering 100x160 μm^2. After stitching of high resolution images (53), 300 cells were identified, and 60 were randomly chosen for cell size estimation, leading to 95% confidence interval on the average cell radius below 0.5 μm. Due to their elliptical shape, the mean radius was estimated as half of the average of their large and small sides, as measured with ImageJ.

Data Analysis

Preliminary post-processing steps included co-registration of DWI scans using an in-house routine (Matlab, the Natick) in order to compensate for potential motion of the animal/sample. Regions of Interests (ROIs) were manually drawn in all 8 mice to delineate the tumor inside the mouse brain on ADC maps derived at oscillation frequency f_{OGSE} = 225 Hz that provided maximal contrast between tumor and normal brain. At voxel level, in vivo and ex vivo high frequency OGSE data (f_{OGSE} > 88 Hz) were first spatially smoothed (3x3 square kernel) and the diffusion coefficient $D(\omega)$ fitted to Eq. [6] in order to determine the free diffusivity D_0 in the short time regime. The diffusion coefficient obtained with low-frequency OGSE (f_{OGSE} < 88 Hz) and PGSE (6 < τ < 31 ms) was then fitted at once to Eqs.

[8b] and [8c] in order to determine the structural parameters ECS and R_{cell} and the apparent extracellular diffusivities D_{ecs} inside the tumor. The intracellular free diffusivity D_{ics} was fully determined by ECS, D_0 and $D_{0,ecs}$ according to Eq. [8a]. The free extracellular diffusivity in the short time limit $D_{0,ecs}$ was fixed at 2.7 μm^2/ms (90% of water free diffusivity at 37°C). Two tailed unpaired Student's t-tests were performed to assess the difference in the mean estimates between in vivo and ex vivo data, due to potential differences in slice location and thickness (1.5 vs 0.1 mm for in vivo and ex vivo, respectively).

Spearman correlation coefficients were calculated between ECS, R_{cell}, D_{ics}, D_{ecs}, and the diffusion values calculated at different diffusion times $\tau = \Delta_{PGSE}$ = 6/9/16/31 ms and oscillation frequencies f_{OGSE} = 65/75/88/100/125/140/160/180/200/225 Hz. The data analysis was performed using in-house Matlab codes (Mathworks, Natick, MA).

Validation of the constant D_{ecs} approximation in the long time limit

Estimations inside spheres of various radii (based on Eq. [5]) suggest that the intracellular diffusion calculated for long times with PGSE ($\tau \gg R_{cell}^2/D_{ics}$) has already reached its long-time limit. In this regime, the mean square displacement $\langle x^2 \rangle = 6 * D(\tau) * \tau$ is constant and the intracellular difusion can be approximated by Eq. [7] with $D_{ics}^{\infty}=0$ (R_{cell} = 4 μm, R^2=0.98). Would that limit be achieved for our PGSE measurements, Eq. [3] simplifies at infinite times with $D_{ics}^{\infty}=0$, and D_{ecs}^{∞} provides a lower bound for the constant diffusivity D_{ecs} attributed to the ECS during the POMACE non-linear fitting to the PGSE and low-frequency OGSE data.

As both the in vivo and ex vivo PGSE data adhere very well to the 1/t asymptotic dependence, these data were fitted to Eq. [7] at tumor level (n=8). Based on high coefficients of determination R^2, D^{∞} was extracted and converted to D_{ecs}^{∞} using the mean ECS estimation (based on Eq. [9]) inside the tumor.

In addition, D_{ecs} (f = 88 Hz) was calculated at tumor level (n=8) using Eq. [6] with $D_{0,ecs}$ =2.70 / 1.94 μm^2/ms (in vivo / ex vivo) and S/V estimates in the short-time regime to provide a superior bound for D_{ecs} in the range f_{OGSE} < 88 Hz. The independently obtained D_{ecs} (f = 88 Hz) and D_{ecs}^{∞} distributions were compared using non parametric tests (Mann-Whitney U test, n=8) in order to justify the use of a constant diffusion in the ECS in the range f_{OGSE} < 88 Hz.

ECS estimation via the Effective Medium Theory

Monte Carlo simulations performed for various geometrical shapes in two dimensions (54) have shown that the two-dimensional analog of Eq. [9] holds well for low cell packing (ECS > 40 %); furthermore, the mean-field theory approach used to deriving this result is generally expected to hold better for higher spatial dimensions. Therefore, we believe its application to tumors prone to necrosis is at least minimally justified; ultimately, its results still need to be independently validated (as we do here by comparing it with the approach based on Eqs. [8]).

PGSE-based D^{∞} extrapolations (from Eq. [7]) were performed at voxel level, converted to *ECS* maps using Eq. [9] with $D_{0,ecs}$= 2.70 or 1.94 μm^2/ms for in vivo or ex vivo (based on PBS measurements), respectively, and compared to the *ECS* estimates derived with POMACE using the combination of PGSE and low frequency OGSE data.

RESULTS

Uncertainty in parameter estimation

Noise propagation was used to assess the uncertainty in estimation of the POMACE model parameters. The four parameters (*ECS*, R_{cell}, D_{ics}, and D_{ecs}) estimated by fitting the above model to the simulation data had *bimodal distributions* with their modes away from their nominal values (see blue distributions Fig. 2B–E). For D_{ics} and D_{ecs}, the two modes correspond to the case where intra- and extracellular diffusivities are equal or when they are constrained by boundary conditions (D_{ecs}< 3 μm^2/ms).

The approach of constraining *ECS* and D_{ics} by fixing $D_{0,ecs}$ using Eq. [8a] during the estimation resulted in unimodal distributions of all four parameters with their modes close to the nominal values, (Fig. 2B–E, black distributions and red line). For SNR=50 (Fig. 2A, typical SNR for ex vivo experiments ~60), the median values of the four parameters (*ECS*, R_{cell}, D_{ics} and D_{ecs}) were 4.5 %, 0.1 %, 1.8 %, and 7.2 % off from the nominal values and the coefficients of variation (CV = standard deviation/mean, or interquartile range/median) are 5, 8, 5, and 13 %, respectively. A two-fold increase/decrease in SNR (SNR=100/25, data not shown) resulted in an equivalent twofold decrease/increase on the CV compared to SNR=50, suggesting an increased precision on the estimation of in vivo parameters (typical in vivo SNR ~ 120) and validating this approach in vivo and ex vivo.

Characterization of tumor micro-environment (*ECS*, R_{cell}, D_{ics}, D_{ecs})

The time-dependence of the diffusion coefficient obtained in vivo with low-frequency OGSE data (f_{OGSE} < 88 Hz) and PGSE data (Fig. 3A) was fitted to Eq. [8b] and [8c], respectively, in order to extract parametric maps of *ECS*, R_{cell}, D_{ics} and D_{ecs} in the tumor (Fig. 3B–E, first line). For visualization purposes, the OGSE dataset was attributed to an equivalent diffusion time τ_{eq} = 1/4 f_{OGSE}, as in (51). This process was repeated for the ex vivo experiment on thin brain sections inserted in the MR histocoil. Representative examples of ex vivo parametric maps are illustrated in Fig. 3B–E (bottom line). Regions of elevated *ECS* (>70%) are highlighted white in *ECS* maps (Fig. 3B).

The tumor area used for MRI analysis (number of voxels × in-plane spatial resolution) was respectively 7.0 ± 5.0 mm^2 and 10.2 ± 7.5 mm^2 for in vivo and ex vivo (n=8). The mean distributions of *ECS*, R_{cell}, D_{ics} and D_{ecs} in the tumor are presented in Table 1. In vivo and ex vivo mean R_{cell} measurements were consistent with each other (4.8 and 4.4 μm). Individual voxel values ranged from 2.5 to 44 μm. A two-fold factor was found between D_{ecs} and D_{ics}, in vivo and ex vivo. In addition, D_{ics} and D_{ecs} were similarly affected by the lower temperature in ex vivo MRI (−16/−21 %). Differences between in vivo and ex vivo diffusivities were smaller than the differences expected due to temperature difference (−30%

in PBS), suggesting changes at cytoplasmic level. Interestingly, the ex vivo data provided higher *ECS* estimates (ΔECS=10 %, P<0.01) than the in vivo data acquired at 37 °C.

At tumor level (n=8), a small correlation was found between tumor size and mean cell radius (Spearman correlation coefficient ρ = 0.4), and between tumor size and cell radius standard deviation within the tumor (ρ = 0.65). The mean cell radius for small / large tumors (analysis area below / above 100 voxels, i.e. 6.25 mm^2) was 3.8 ± 0.7 and 5.2 ± 1.8 μm, respectively.

Extracellular diffusivity in the long time regime

The long time limit is well characterized by a linear relationship between $D(\tau)$ and $1/\tau$ (24). As illustrated in Fig. 4A–B, a very good agreement was found between the functional form - Eq. [7] - characterizing this regime and both the in vivo (Fig. 4A, R^2=0.89±0.11) and ex vivo (Fig. 4B, R^2=0.98±0.02) PGSE data. Based on this result, the extrapolation of the PGSE data to infinite diffusion times (D^∞) provides an estimation $D_{ecs}^{\infty}=D^{\infty}/ECS$ for the extracellular diffusivity at infinitely long times.

From the short-time regime, following Eq. [6], with surface to volume ratio S/V = 0.57 ± 0.05 // 0.34 ± 0.04 μm^{-1} (n=8) and $D_{0,ecs}$ = 2.70 // 1.94 μm^2/ms (in vivo // ex vivo), we find D_{ecs} (f = 88 Hz) = 1.90 ± 0.09 and 1.64 ± 0.03 μm^2/ms, in vivo and ex vivo respectively.

The comparison of the D_{ecs}, D_{ecs} (f = 88 Hz) and D_{ecs}^{∞} distributions is presented in Fig. 4C. Based on the model-free extrapolation of the PGSE data, D_{ecs}^{∞} was not found significantly different (Mann-Whitney U test, P=0.16) from D_{ecs} (f = 88 Hz) (Fig. 4C, 1.83 ± 0.09 vs. 1.90±0.09 μm^2/ms) in vivo. Similarly, no significant difference (Mann-Whitney U test, P=0.80) was found between the ex vivo D_{ecs} (f = 88 Hz) and D_{ecs}^{∞} (Fig. 4C, right columns, 1.64±0.04 vs. 1.60±0.18 μm^2/ms). These results suggest that the true extracellular diffusivity is not varying much in our time- or frequency range (maximum 3% difference between the average D_{ecs} (f = 88 Hz) and D_{ecs}^{∞}) and can be considered constant when modeling the tumor micro-environment in the diffusion time / oscillation frequency range used in this study: f < 88 Hz and τ< 31 ms.

Correlation with Diffusion Metrics

Table 2 shows the correlation coefficients ρ between one of the POMACE parameters (*ECS*, R_{cell}, D_{ics}, D_{ecs}) and conventional DWI metrics - $D(\omega)$ or $D(t)$ at four different frequencies/ times as representative examples. The complete tables (14 frequencies / times, in vivo / ex vivo) can be accessed online in the supporting materials (Table S1–2). *ECS* was found mainly correlated with diffusion coefficients obtained with PGSE (Table 2, bold in first two columns), supporting the link between long time diffusion and cellularity. On the other hand, the correlation between D_{ics} and $D(\tau)$ increased mildly as the diffusion time decreased / frequency increased (ρ =0.74/0.62 for f_{OGSE}=225 Hz). R_{cell} and D_{ecs} were not found strongly correlated to any of the diffusion metrics.

EMT-based *ECS* mapping

The comparison of voxel-based *ECS* distributions is presented in Table 3. As illustrated in Fig. 5A & B, mean in vivo values of both models were 44 %. Coefficients of variation were

lower for EMT (CV = 11 vs. 16%), as reflected by more homogeneous *ECS* maps (Fig. 5B). Similar results were found with the ex vivo data (mean ex vivo *ECS* = 54 % vs. 56 %, CV = 13 vs. 20 %). Both *ECS* metrics were found strongly correlated at voxel level (Fig. 5C, ρ =0.64 / 0.84, in vivo / ex vivo, blue / red) with a slope close to unity (Fig. 5C, dy/dx=0.87 vs. 1.0, dotted vs. plain line).

Histology

Due to high heterogeneity within the tumor and mechanical distortions during tissue preparation, different features were observed in the brain sections used for ex vivo MRI compared to the adjacent sections used for immunohistochemistry (IHC) (5 μm thickness), making it non-trivial to directly correlate *ECS* maps with IHC. In some cases, areas of various cell density could be detected in the tumor, which appear to match with the pattern of *ECS* estimated using MRI. Due to the mismatch between IHC and MRI sections, optical microscopy was preferred to IHC for the validation of ex vivo *ECS* maps.

Optical Microscopy

Microscopy (Fig. 6A–C) was performed without additional staining on the same brain sections used for ex vivo MRI (Fig. 5A–B, ex vivo panel) in order to prevent mismatch due to tissue fixation, distortion, and slice thickness. As a result, microscopic images appeared blurry at cellular level, as several cellular layers (R_{cell}<10 μm) were superimposed within the 100 μm brain section. At tumor level, a good correlation was found between the necrotic areas observed with microscopy (indicated by the black and white arrows in Fig. 6) and the locations of high *ECS* based on ex vivo MRI (white areas in Fig. 5A–B, *ECS* > 70%). Similarly, regions of low *ECS* appear to match areas of tumor infiltration in gray and white matter located near the rim of the tumors. These results, made possible via the use of an MR histocoil, could suggest that the *ECS* values obtained using the time-dependence of the diffusion coefficient accurately depict the structural organization of the tumor at cellular level.

Electron Microscopy

The tumor cell radius was measured using EM images (see Fig. S3A–B in supplementary materials). A representative raw EM image with corresponding cell delineation can be found online (supplementary materials, Fig. S3). From the 60 cells randomly chosen in the tumor, the estimated radius was 4.7 ± 1.7 μm (with 0.4 μm 95% confidence interval on the mean cell radius), which is in good agreement with the R_{cell} estimated using in vivo and ex vivo MRI (4.8 ± 1.3 // 4.3 ± 1.4 μm). Interestingly, both methods provided very similar results for the cell dimensions despite potential structural changes due to the different tissue fixation methods required prior to EM imaging or ex vivo MRI.

DISCUSSION

Our results demonstrate that the proposed POMACE framework can be used to gain insight into the tumor microenvironment. Using a simple model of impermeable spheres for cancer cells, the extracellular space and cell radius can be quantified and used to characterize the tumor microstructure. Our *ECS* measurements, in agreement with *ECS* literature in brain

tumors (see Table 1 in (1)), reflected the dramatic changes in *ECS* observed with optical microscopy on the same samples. In particular, micro-necrotic regions were easily detected using MRI. In vivo and ex vivo estimates of the cell radius were consistent, and in agreement with that measured in EM images of the same cell line, suggesting this method can be applied to estimate cell size in vivo non-invasively.

The approximation used to identify the ADC as the diffusion coefficient in Eq. [3] was checked retrospectively. Since D_{ics} and D_{ecs} estimates are on the order of 1.0 and 2.7 μm^2/ms, a slight non-Gaussianity arises from the linear combination of MRI signals when b≠0. This can be calculated, numerically from the comparison of $D=ECS*D_{ecs}+(1-ECS)*D_{ics}$ with $ADC=-\log(S_{total})/b$, or equivalently from assessing the second-order term (b^2) in the Taylor expansion of the overall MRI signal: $\Delta D = (b/2)*ECS*(1-ECS)*(D_{ecs}-D_{ics})\hat{}2$, resulting in both cases in an overall 8% relative difference at b=0.4 ms/μm^2. These errors were found below the accuracy of our diffusion measurements, which were on average and at voxel level 10 ± 9 %.

Realistic modeling of tumor tissue is complex. The functional form of the time-dependence of a diffusion coefficient depends on the particular packing and structural disorder of the medium (24,55,56), which is unknown. It is tempting to tackle this fundamental problem by probing the extremely short and/or long time limit, where the functional form of the time-dependence is known. In those regimes, several physical parameters can in addition be neglected and/or simplified.

In the very short time regime, the cellular micro-architecture (including cell size, shape and packing) can be simply characterized by the surface-to-volume ratio S/V of the cell walls, and the diffusion time-dependence is fully expressed by two independent parameters: D_0 and S/V (44,46). D_0 represents the medium free diffusivity (in absence of restrictions) and S/V the purely geometrical restrictions. Although promising via its link to cellularity, the utility of this approach to characterize cancer remains to be investigated. The extension of this work to larger tumor cells, as described in (26), should be straightforward, as most of the time-dependence occurs at lower frequencies that are easily probed on preclinical scanners. In contrast, in *healthy brain structures*, such as gray or white matter, very high oscillation frequencies (f_{OGSE} > 1kHz) are required to probe the Mitra regime due to smaller cellular sizes (19); feasible diffusion times using an MRI system similar to what used in our study correspond to the long time asymptotic approach of the tortuosity limit as both axons and dendrites are very narrow.

In the long time regime, the diffusion coefficient $D(\tau)$ in three-dimensional random media reaches towards its asymptotical limit D^{∞} as $1/\tau$; in our case, this behavior should describe the extra-cellular diffusivity. Since the intracellular diffusion becomes fully constrained by cellular membranes, the corresponding intracellular diffusivity approaches zero also as $1/\tau$. This justifies the usage of Eq. [7] to determine the overall tortuosity asymptote. Practically, in the absence of strong variations of the extracellular medium, numerous studies have used a PGSE-based ADC as a successful inverse surrogate for cell density (11,13,57).

Here it is important to note that it is the three-dimensional random packing geometry that allows us to use the simple extrapolation formula [7] and to not model the time dependence in the extra-cellular space explicitly. Generally, one should be careful to investigate the role of time dependence in the extra-cellular space. For example, in the two-dimensional random packing geometry of diffusion transverse to axonal tracts, the corresponding extra-cellular diffusivity approaches its tortuosity limit much slower, as $(\ln \tau)/\tau$ (19), than the $1/\tau$ approach (24) in the three-dimensional random geometry. As a result, diffusion time dependence in the extra-axonal space has been recently shown to provide the dominant contribution to the overall time dependence, and to strongly confound axonal diameter estimates (19,20). Recent study shows that including the extracellular diffusivity time dependence leads to axonal diameter estimates about 3–5 smaller than when the time dependence is not included, which in turn makes the estimated diameter values below the practical detection limit (58).

Approaching the long-time regime with PGSE was used here as a tool to (1) extrapolate towards the tortuosity limit D^{∞} which is, formally speaking, experimentally unreachable; and (2) validate the assumption of a constant diffusivity in the ECS in our range of times and frequencies. Note that the latter required only limited prior knowledge on cell size ($R_{cell} < 8$ μm) in addition to the POMACE assumptions (impermeable membranes and free extracellular diffusivity = 2.7/1.94 μm^2/ms in vivo / ex vivo). Results were highly encouraging, as a maximum 10% relative difference was found between D_{ecs} (f_{OGSE} = 88 Hz) and this long time limit D_{ecs}^{∞}. These small D_{ecs} changes outside the short-time regime were found consistent with EMT-based D_{ecs}^{∞} estimates, following Eq. [9] and ECS literature in brain glioma (see Table 1 in (1)). Large ECS volume fractions (~50 %) lead indeed to elevated ratios $D_{ecs}^{\infty}/D_{0,ecs} = \sqrt{ECS} \sim 0.70$, comparable with $D_{ecs}/D_{0,ecs}$ estimations from the short-time regime (Eq. [6]) using realistic ECS parameters ($D_{0,ecs}$=2.7 μm^2/ms, S/V=0.4 μm^{-1}) and oscillation frequency ($D_{ecs}/D_{0,ecs}$ = 0.76 at f_{OGSE} = 88 Hz). Based on this, all of the time dependence of the diffusion coefficient in the range [1/(88 Hz) – 31 ms] was entirely attributed to intracellular restrictions, and ECS and R_{cell} unambiguously extracted from Eq. [8b–c]. For this purpose, estimations based on Eq. [8b] suggested that the diffusion times used in this study ($6 < \tau < 31$ ms) were sufficient to consider that the long time regime was reached inside the cells (D linear with $1/\tau$).

In principle, if our time-independent approximation for ECS diffusivity does not hold, the time-dependence of the diffusion in the ECS would need to be accounted for when fitting $D(\omega)/D(\tau)$. This can be problematic, as fits become extremely unstable when allowing for D_{ecs} to vary with frequency or time. For PGSE this is due to the very similar functional forms of intra- and extracellular diffusivities approaching the long time regime (see Eq. [7]). As a result, these compartments cannot be resolved in the absence of strong constraints. Another way to effectively constrain fitting is acquiring higher-order diffusion metrics such as kurtosis terms; however, this requires stronger diffusion weighting and extra scan time. Five-parameter models (combining OGSE at 40 and 80 Hz and a single PGSE with τ=52 ms) were shown successful in identifying cell pellets of various size (R_{cell}=10/20 μm) (27). However, only relative ECS changes could be demonstrated in solutions of various but unknown cellular densities. Since their model assumes constant diffusivity in the ECS for PGSE, the ECS quantification accuracy would benefit from additional PGSE measurements

in this intermediate range. In general, the ECS diffusion time-dependence can only be neglected under certain circumstances (specific time range vs. cellular dimensions, low cellular packing, dimensionality of the problem – in particular, 3 dimensions is much more favorable in this respect than 2 dimensions), that must be thoroughly investigated and validated. In addition, for longer diffusion times, recent studies (39) suggest that the influence of cellular permeability on the measured diffusion coefficient cannot be neglected and should be accounted for in Eq. [4–5]. This constitutes a minor limitation to our study, as only the longest diffusion time (31 ms) was near the boundary of the range safe to assume cells can be considered impermeable (around one-tenth of the water residency time) (38–41). With the multiple shorter diffusion times using PGSE, Δ=6, 9, and 16 ms, which are less likely affected by the exchange effect, we expect that the error induced by a potential small bias in the fit due to the measurement at Δ=31ms is not considerably large.

In general, particular caution was taken to ensure the validity of the many assumptions used throughout this study. In addition to pilot studies investigating IVIM effects and diffusion isotropy in the tumor, MR parameters were fixed when possible. Only the diffusion time / period and number of oscillations were allowed to vary during the experiment. Small and constant *b*-values ([0–0.4] ms/ μm^2) ensured that the mono-exponential "DTI" regime was maintained and additional orders of the MR signal cumulant expansion (33) could be neglected for all diffusion times / frequencies. Similarly, TE and TR values were kept constant (70/3000 ms) to minimize the influence of potential different relaxation times in the two compartments.

Ex vivo diffusivities were found significantly smaller than in vivo, although the experimental difference (D_{PGSE}, D_0, D_{ics} and D_{ecs} decreased by 15, 25, 20 and 16 %, respectively) did not reach the expected decrease due to temperature between 37 and 20 degrees (−30 %, as measured in PBS). Since cellular size were found similar in vivo and ex vivo, these changes must be explained by changes at microstructural level triggered during the fixation process and impacting cellular permeability and/or ECS content, such as the removal of small extracellular structures during the fixation process. It was beyond the scope of this study to determine the exact underlying changes caused by the tissue preparation for ex vivo experiment. However, because there can be substantial differences between in vivo MRI and histopathological assessment for the same reason, the ex vivo MRI experiment was included for cross-validation of the model with other ex vivo methods in this study.

The two approaches to quantify the *ECS* in vivo and ex vivo (low-frequency OGSE+PGSE vs. EMT) provided very similar results in the tumor. In addition, both methods matched well with the structural information extracted from the ex vivo microscopy data, suggesting both methods are suitable to extract the true extracellular fraction. EMT-based *ECS* maps were found in general more homogeneous, likely to be a result of the lesser number of fit parameters. However, combining diffusion at different scales (OGSE+PGSE) provided an additional estimate of the cellular radius R_{cell}, while D^{∞} extrapolation in the long time limit is - for impermeable structures - independent of cell size (49). In addition, the EMT assumes that the extracellular diffusivity $D_{0,ecs}$ is homogenous and unconstrained, while the "apparent" constant diffusivity D_{ecs} is allowed to vary in the other model. The latter could constitute an advantage in situations prone to changes in the extracellular medium, such as

post-injury states or ischemia (59). Here should be noted that, since both techniques make similar assumptions – the validity of which is discussed earlier -, they do not provide fully independent ECS estimation.

Both MRI-based *ECS* quantification approaches highlighted an increase of the *ECS* (average ΔECS=+10%) ex vivo. This result is counterintuitive, as brain structures (including the extracellular matrix) are known to shrink under the influence of tissue fixatives used for sample preparation (60). This cellular shrinkage process remains however small after PFA fixation (61) and tumor expansion could be facilitated by the skull removal and rehydration process, partially releasing tumor interstitial pressure. In addition, we cannot exclude partial removal of low packed cells during the fixation and sectioning process, explaining why our data did not support evidence of ECS shrinkage due to tissue fixation. Additional ex vivo measurements prior to tissue sectioning would help answer this question.

The validation of the *ECS* estimates was made possible by using a histocoil (52) allowing for the imaging of very thin brain slices (100 μm) that could be imaged using a different modality (optical microscopy in this case). In addition, sufficient SNR was maintained all around the sample (in vivo / ex vivo SNR = 120/60) to derive parametric maps despite a fifteen-fold decrease in slice thickness. Another utility of the histocoil lies in the possibility to perform ex vivo MRI at various temperatures. This can be used as an additional tool to probe different diffusion time regimes (37).

Despite providing the right order of magnitude for cell size, EM cell size measurements were only performed in one animal and limited number of cells (n=60), which might not be representative of the full cohort. In addition, the estimation method used in this study would lead to cell size underestimation for highly aspherical cells intersecting the EM imaging plane. To date, direct correlation of MRI and EM is not possible due to differences in slice thicknesses and tissue preparation, justifying this approach to estimate cell size. Since MRI estimates only pointed out a small difference in mean cell radius between small and large tumors (3.8 vs. 5.2 μm), any bias when comparing EM performed at 14 days and MRI estimates obtained between 14–28 days would remain small.

Kucheryavykh et al (62) reported that the radius distribution becomes larger at the later stage of tumor growth to (15–60 um in diameter). Similarly, Resende et al (63) reported that GL261 size was around 10–20 um in diameter at the early stage and increases to 14–52 um in the later stage of about 3 weeks post tumor implantation. These two studies were conducted with brain slices, whereas our study was based on the measurement of tumor in the intact brain. In this study, we found a weak correlation between tumor size and mean cell radius (ρ = 0.4) and a stronger correlation between tumor size and cell radius standard deviation within the tumor (ρ = 0.65), suggesting cancer cells could indeed become larger at later stage, but the mean cell radius remained on the same order of magnitude (R_{cell} = 3.8 ± 0.7 vs. 5.2 ± 1.8 μm for the small and large tumors). Despite this difference in experimental conditions, the estimated cell radius from our study is quite close to the ex vivo measurements that can be appreciated in supplementary Figure S3.

The quantitative comparison of MRI- and IHC-based *ECS* estimates failed due to differences in structure between two consecutive brain sections of different thicknesses (100 vs. 5 μm). Although qualitative comparisons on several neighboring slices support the validity of MRI-*ECS* measurement, a rigorous multimodal correlation can only be achieved via consecutive MRI and IHC of thin brain sections (5–10 μm). This would however degrade MR performances and generate additional diffusion restrictions in the sample. This problem can be solved using 3D ex vivo MRI followed by histology, provided the tissue integrity is well preserved during preparation and sectioning.

Although the ECS can also be estimated from DCE-MRI, the accuracy of ECS measurement in DCE-MRI can be affected by multiple factors, such as arterial input function, tissue Gd relaxivity, pre-contrast T1, RF coil sensitivity, and water exchange between vascular, intra- and extracellular compartments (64). It is beyond the scope of our study to include another MRI modality with its own uncertainty in measuring ECS. Future studies are needed to compare the POMACE-measured ECS with that of DCE-MRI.

Other diffusion models relevant for cancer studies have used the vascular compartment directionality (26), exchange rate (65) or micro FA approach (66) in order to characterize tumor microstructure, often at the expense of accurate extracellular space quantification. On the other hand, the present technique focuses on estimation of the cell size and extracellular space fraction, which has been recognized as a strong biomarker for treatment efficacy (1).

The proposed method in this study can be translated to clinical scanners with additional restrictions on the OGSE frequency range depending on the gradient hardware limitations. The geometrical model would also remain valid for various brain tumors as the size of human cancer cells are in the same order of magnitude as those of the murine glioma cells used in this study. The OGSE frequency and diffusion time ranges can be adjusted in order to optimize the measurement condition for the specific size of any particular cancer type. However, it should be stressed that the proposed method cannot be applied to the normal brain tissues even in the mouse brain, as some of the fundamental assumptions (directionality, cell size, geometry, packing density) used for our method may not be valid. Smaller neuronal structures require a substantially higher range of oscillating gradient frequencies to achieve sufficiently short time range to estimate S/V. A higher packing density in normal brain compared to glioma is another critical factor that affects the approximation of negligible diffusion time-dependence in the ECS. In addition, many of murine brain regions, including the cortical ribbon, have structural alignment that gives a rise to diffusion anisotropy. Hence, assessment of time-dependence of diffusion in normal brain tissue requires a considerably different approach than the method proposed in this study. In fact, one of the motivations for this study was to develop a specific measurement method appropriate for cancer cells given their differences from normal brain tissue.

The model analysis in the proposed method is based on the ADC values at individual diffusion times and oscillating gradient frequencies, such that it is not directly affected by many of the acquisition parameters. The most critical parameter for the model is the diffusion time and frequency range as it is supposed to include both short-time AND long-time regimes for cancer cells. As long as the data acquisition includes multiple

measurements in these two regimes for our target tissue, we do not expect that the choice of individual diffusion times and frequencies would influence the outcome of the analysis. In this study, the diffusion times and frequencies were chosen to cover the whole available spectrum, thus ensuring maximal sensitivity to the diffusion time-dependence. Future study is warranted to further investigate and optimize the selection of the diffusion times for characterization of cancer cells.

In summary, it is possible to characterize the tumor microenvironment inside a loosely packed mouse glioma cells both in vivo and ex vivo, using the time-dependence of the diffusion coefficient and a simple model of impermeable spheres when appropriate diffusion times are used. The combination of PGSE and OGSE data and the proposed POMACE framework of analysis provide a quantitative means to estimate both the cell radius and extracellular space fraction, that can be used as non-invasive MRI markers to assess micro-necrotic areas, modification of the extracellular matrix, tumor progression or treatment response.

Supplementary Material

Refer to Web version on PubMed Central for supplementary material.

Acknowledgments

This work was supported in part by NIH R01CA160620 and was performed under the OCS Preclinical Imaging Core partially funded by the NYU Laura and Isaac Perlmutter Cancer Center Support Grant, NIH/NCI P30CA016087. The Center for Advanced Imaging Innovation and Research (CAI^{2}R, www.cai2r.net) at New York University School of Medicine is supported by NIH/NIBIB P41 EB017183.

Abbreviations

ADC	Apparent Diffusion Coefficient
CV	Coefficient of Variation
DCE	Dynamic Contrast Enhanced MRI
DTI	Diffusion Tensor Imaging
ECS	extracellular space
EM	Electron Microscopy
EMT	Effective Medium Theory
GL261	mouse Glioma 261
GLUT1	Glucose Transporter 1
IHC	Immuno-histochemistry
PB(S)	Phosphate Buffered (Saline) solution
PFA	Paraformaldehyde

POMACE	Pulsed and Oscillating gradient MRI for Assessment of Cell Size and Extracellular space
PGSE/OGSE	Pulsed/Oscillating Gradient Spin Echo
ROI	Region of Interest
S/V	Surface-to-Volume ratio

References

1. Jain RK. Transport of Molecules in the Tumor Interstitium - a Review. Cancer Res. 1987; 47(12): 3039–3051. [PubMed: 3555767]
2. Milosevic M, Fyles A, Hedley D, Pintilie M, Levin W, Manchul L, Hill R. Interstitial fluid pressure predicts survival in patients with cervix cancer independent of clinical prognostic factors and tumor - Oxygen measurements. Cancer Res. 2001; 61(17):6400–6405. [PubMed: 11522633]
3. Rofstad EK, Tunheim SH, Mathiesen B, Graff BA, Halsor EF, Nilsen K, Galappathi K. Pulmonary and lymph node metastasis is associated with primary tumor interstitial fluid pressure in human melanoma xenografts. Cancer Res. 2002; 62(3):661–664. [PubMed: 11830516]
4. Yu T, Wang Z, Liu K, Wu Y, Fan J, Chen J, Li C, Zhu G, Li L. High interstitial fluid pressure promotes tumor progression through inducing lymphatic metastasis-related protein expressions in oral squamous cell carcinoma. Clin Transl Oncol. 2014; 16(6):539–547. [PubMed: 24085575]
5. Sun L, Sakurai S, Sano T, Hironaka M, Kawashima O, Nakajima T. High-grade neuroendocrine carcinoma of the lung: comparative clinicopathological study of large cell neuroendocrine carcinoma and small cell lung carcinoma. Pathology international. 2009; 59(8):522–529. [PubMed: 19627535]
6. Brauer M. In vivo monitoring of apoptosis. Progress in neuro-psychopharmacology & biological psychiatry. 2003; 27(2):323–331. [PubMed: 12657370]
7. Sykova E, Nicholson C. Diffusion in brain extracellular space. Physiological reviews. 2008; 88(4): 1277–1340. [PubMed: 18923183]
8. Nicholson C, Tao L. Hindered diffusion of high molecular weight compounds in brain extracellular microenvironment measured with integrative optical imaging. Biophysical journal. 1993; 65(6): 2277–2290. [PubMed: 7508761]
9. Sykova E. Extrasynaptic volume transmission and diffusion parameters of the extracellular space. Neuroscience. 2004; 129(4):861–876. [PubMed: 15561404]
10. Hayashida Y, Yakushiji T, Awai K, Katahira K, Nakayama Y, Shimomura O, Kitajima M, Hirai T, Yamashita Y, Mizuta H. Monitoring therapeutic responses of primary bone tumors by diffusion-weighted image: initial results. Eur Radiol. 2006; 16(12):2637–2643. [PubMed: 16909220]
11. Padhani AR, Liu G, Koh DM, Chenevert TL, Thoeny HC, Takahara T, Dzik-Jurasz A, Ross BD, Van Cauteren M, Collins D, Hammoud DA, Rustin GJ, Taouli B, Choyke PL. Diffusion-weighted magnetic resonance imaging as a cancer biomarker: consensus and recommendations. Neoplasia. 2009; 11(2):102–125. [PubMed: 19186405]
12. Kim S, Loevner L, Quon H, Sherman E, Weinstein G, Kilger A, Poptani H. Diffusion-Weighted Magnetic Resonance Imaging for Predicting and Detecting Early Response to Chemoradiation Therapy of Squamous Cell Carcinomas of the Head and Neck. Clin Cancer Res. 2009; 15(3):986–994. [PubMed: 19188170]
13. Manenti G, Di Roma M, Mancino S, Bartolucci DA, Palmieri G, Mastrangeli R, Miano R, Squillaci E, Simonetti G. Malignant renal neoplasms: correlation between ADC values and cellularity in diffusion weighted magnetic resonance imaging at 3 T. Radiol Med. 2008; 113(2): 199–213. [PubMed: 18386122]
14. Xu JZ, Does MD, Gore JC. Quantitative characterization of tissue microstructure with temporal diffusion spectroscopy. J Magn Reson. 2009; 200(2):189–197. [PubMed: 19616979]

15. Gore JC, Xu JZ, Colvin DC, Yankeelov TE, Parsons EC, Does MD. Characterization of tissue structure at varying length scales using temporal diffusion spectroscopy. Nmr Biomed. 2010; 23(7):745–756. [PubMed: 20677208]
16. Aggarwal M, Jones MV, Calabresi PA, Mori S, Zhang JY. Probing mouse brain microstructure using oscillating gradient diffusion MRI. Magn Reson Med. 2012; 67(1):98–109. [PubMed: 21590726]
17. Portnoy S, Fichtner ND, Dziegielewski C, Stanisz MP, Stanisz GJ. In vitro detection of apoptosis using oscillating and pulsed gradient diffusion magnetic resonance imaging. Nmr Biomed. 2014; 27(4):371–380. [PubMed: 24421173]
18. Portnoy S, Flint JJ, Blackband SJ, Stanisz GJ. Oscillating and Pulsed Gradient Diffusion Magnetic Resonance Microscopy Over an Extended b-Value Range: Implications for the Characterization of Tissue Microstructure. Magnetic Resonance in Medicine. 2013; 69(4):1131–1145. [PubMed: 22576352]
19. Burcaw LM, Fieremans E, Novikov DS. Mesoscopic structure of neuronal tracts from time-dependent diffusion. NeuroImage. 2015; doi: 10.1016/j.neuroimage.2015.03.061
20. Fieremans E, Burcaw LM, Lee HH, Lemberskiy G, Veraart J, Novikov DS. In vivo observation and biophysical interpretation of time-dependent diffusion in human white matter. NeuroImage. 2016; 129:414–427. [PubMed: 26804782]
21. Cleveland GG, Chang DC, Hazlewood CF, Rorschach HE. Nuclear magnetic resonance measurement of skeletal muscle: anisotrophy of the diffusion coefficient of the intracellular water. Biophysical journal. 1976; 16(9):1043–1053. [PubMed: 963204]
22. Kim S, Chi-Fishman G, Barnett AS, Pierpaoli C. Dependence on diffusion time of apparent diffusion tensor of ex vivo calf tongue and heart. Magn Reson Med. 2005; 54(6):1387–1396. [PubMed: 16265644]
23. Sigmund EE, Novikov DS, Sui D, Ukpebor O, Baete S, Babb JS, Liu K, Feiweier T, Kwon J, McGorty K, Bencardino J, Fieremans E. Time-dependent diffusion in skeletal muscle with the random permeable barrier model (RPBM): application to normal controls and chronic exertional compartment syndrome patients. Nmr Biomed. 2014; 27(5):519–528. [PubMed: 24610770]
24. Novikov DS, Jensen JH, Helpern JA, Fieremans E. Revealing mesoscopic structural universality with diffusion. P Natl Acad Sci USA. 2014; 111(14):5088–5093.
25. Murday JS, Cotts RM. Self-Diffusion Coeffcient of Liquid Lithium. J Chem Phys. 1968; 48(11): 4938.
26. Panagiotaki E, Walker-Samuel S, Siow B, Johnson SP, Rajkumar V, Pedley RB, Lythgoe MF, Alexander DC. Noninvasive Quantification of Solid Tumor Microstructure Using VERDICT MRI. Cancer Res. 2014; 74(7):1902–1912. [PubMed: 24491802]
27. Jiang X, Li H, Xie J, Zhao P, Gore JC, Xu J. Quantification of cell size using temporal diffusion spectroscopy. Magn Reson Med. 2015
28. Fidler IJ. Tumor Heterogeneity and Biology of Cancer Invasion and Metastasis. Cancer Res. 1978; 38(9):2651–2660. [PubMed: 354778]
29. Heppner GH, Miller BE. Tumor Heterogeneity - Biological Implications and Therapeutic Consequences. Cancer Metast Rev. 1983; 2(1):5–23.
30. Almendro V, Marusyk A, Polyak K. Cellular heterogeneity and molecular evolution in cancer. Annual review of pathology. 2013; 8:277–302.
31. Niendorf T, Dijkhuizen RM, Norris DG, Campagne MV, Nicolay K. Biexponential diffusion attenuation in various states of brain tissue: Implications for diffusion-weighted imaging. Magn Reson Med. 1996; 36(6):847–857. [PubMed: 8946350]
32. Mulkern RV, Gudbjartsson H, Westin CF, Zengingonul HP, Gartner W, Guttmann CRG, Robertson RL, Kyriakos W, Schwartz R, Holtzman D, Jolesz FA, Maier SE. Multi-component apparent diffusion coefficients in human brain. Nmr Biomed. 1999; 12(1):51–62. [PubMed: 10195330]
33. Kiselev, VG. The Cumulant Expansion: an Overarching Mathematical Framework for Understanding Diffusion NMR. In: Jones, DK., editor. Diffusion MRI: theory, methods and applications. Vol. Ch 10. Oxford University Press; New York: 2010.

34. Jensen JH, Helpern JA, Ramani A, Lu HZ, Kaczynski K. Diffusional kurtosis imaging: The quantification of non-Gaussian water diffusion by means of magnetic resonance imaging. Magn Reson Med. 2005; 53(6):1432–1440. [PubMed: 15906300]
35. Novikov DS, Kiselev VG. Effective medium theory of a diffusion-weighted signal. Nmr Biomed. 2010; 23(7):682–697. [PubMed: 20886563]
36. Meier C, Dreher W, Lebrfritz D. Diffusion in compartmental systems. I. A comparison of an analytical model with simulations. Magn Reson Med. 2003; 50(3):500–509. [PubMed: 12939757]
37. Reynaud O, Winters KV, Hoang DM, Wadghiri YZ, Novikov DS, Kim SG. Surface-to-volume ratio mapping of tumor microstructure using oscillating gradient diffusion weighted imaging. Magn Reson Med. 2015
38. Springer CS, Li X, Tudorica LA, Oh KY, Roy N, Chui SYC, Naik AM, Holtorf ML, Afzal A, Rooney WD, Huang W. Intratumor mapping of intracellular water lifetime: metabolic images of breast cancer? Nmr Biomed. 2014; 27(7):760–773. [PubMed: 24798066]
39. Li H, Jiang X, Xie J, McIntyre JO, Gore JC, Xu J. Time-dependent influence of cell membrane permeability on MR diffusion measurements. Magn Reson Med. 2015
40. Nilsson M, Latt J, van Westen D, Brockstedt S, Lasic S, Stahlberg F, Topgaard D. Noninvasive mapping of water diffusional exchange in the human brain using filter-exchange imaging. Magn Reson Med. 2013; 69(6):1573–1581. [PubMed: 22837019]
41. Bailey C, Giles A, Czarnota GJ, Stanisz GJ. Detection of apoptotic cell death in vitro in the presence of Gd-DTPA-BMA. Magn Reson Med. 2009; 62(1):46–55. [PubMed: 19253383]
42. Xu J, Does MD, Gore JC. Sensitivity of MR Diffusion Measurements to Variations in Intracellular Structure: Effects of Nuclear Size. Magn Reson Med. 2009; 61(4):828–833. [PubMed: 19205020]
43. Xu JZ, Li H, Harkins KD, Jiang XY, Xie JP, Kang H, Does MD, Gore JC. Mapping mean axon diameter and axonal volume fraction by MRI using temporal diffusion spectroscopy. NeuroImage. 2014; 103:10–19. [PubMed: 25225002]
44. Mitra PP, Sen PN, Schwartz LM. Short-Time Behavior of the Diffusion-Coefficient as a Geometrical Probe of Porous-Media. Phys Rev B. 1993; 47(14):8565–8574.
45. Novikov DS, Kiselev VG. Surface-to-volume ratio with oscillating gradients. J Magn Reson. 2011; 210(1):141–145. [PubMed: 21393035]
46. Latour LL, Mitra PP, Kleinberg RL, Sotak CH. Time-Dependent Diffusion-Coefficient of Fluids in Porous-Media as a Probe of Surface-to-Volume Ratio. J Magn Reson Ser A. 1993; 101(3):342–346.
47. Sukstanskii AL. Exact analytical results for ADC with oscillating diffusion sensitizing gradients. J Magn Reson. 2013; 234:135–140. [PubMed: 23876779]
48. deSwiet TM, Sen PN. Time dependent diffusion coefficient in a disordered medium. J Chem Phys. 1996; 104(1):206–209.
49. Latour LL, Svoboda K, Mitra PP, Sotak CH. Time-Dependent Diffusion of Water in a Biological Model System. P Natl Acad Sci USA. 1994; 91(4):1229–1233.
50. Dazai J, Bock NA, Nieman BJ, Davidson LM, Henkelman RM, Chen XJ. Multiple mouse biological loading and monitoring system for MRI. Magn Reson Med. 2004; 52(4):709–715. [PubMed: 15389955]
51. Parsons EC Jr, Does MD, Gore JC. Temporal diffusion spectroscopy: theory and implementation in restricted systems using oscillating gradients. Magn Reson Med. 2006; 55(1):75–84. [PubMed: 16342147]
52. Hoang DM, Voura EB, Zhang C, Fakri-Bouchet L, Wadghiri YZ. Evaluation of Coils for Imaging Histological Slides: Signal-to-Noise Ratio and Filling Factor. Magn Reson Med. 2014; 71(5): 1932–1943. [PubMed: 23857590]
53. Preibisch S, Saalfeld S, Tomancak P. Globally optimal stitching of tiled 3D microscopic image acquisitions. Bioinformatics. 2009; 25(11):1463–1465. [PubMed: 19346324]
54. Novikov, DS.; Fieremans, E. Relating extracellular diffusivity to cell size distribution and packing density as applied to white matter. Proceedings of the 20th Annual Meeting of ISMRM; Melbourne, Victoria, Australia. 2012. p. 1829
55. Fieremans E, Novikov DS, Jensen JH, Helpern JA. Monte Carlo study of a two-compartment exchange model of diffusion. Nmr Biomed. 2010; 23(7):711–724. [PubMed: 20882537]

56. Novikov DS, Fieremans E, Jensen JH, Helpern JA. Random walk with barriers. Nature physics. 2011; 7(6):508–514. [PubMed: 21686083]
57. Taouli B, Vilgrain V, Dumont E, Daire JL, Fan B, Menu Y. Evaluation of liver diffusion isotropy and characterization of focal hepatic lesions with two single-shot echo-planar MR imaging sequences: Prospective study in 66 patients. Radiology. 2003; 226(1):71–78. [PubMed: 12511671]
58. De Santis S, Jones DK, Roebroeck A. Including diffusion time dependence in the extra-axonal space improves in vivo estimates of axonal diameter and density in human white matter. NeuroImage. 2016; 130:91–103. [PubMed: 26826514]
59. Vorisek I, Hajek M, Tintera J, Nicolay K, Sykova E. Water ADC, extracellular space volume, and tortuosity in the rat cortex after traumatic injury. Magn Reson Med. 2002; 48(6):994–1003. [PubMed: 12465109]
60. Wehrl HF, Bezrukov I, Wiehr S, Lehnhoff M, Fuchs K, Mannheim JG, Quintanilla-Martinez L, Kohlhofer U, Kneilling M, Pichler BJ, Sauter AW. Assessment of murine brain tissue shrinkage caused by different histological fixatives using magnetic resonance and computed tomography imaging. Histology and histopathology. 2015; 30(5):601–613. [PubMed: 25504583]
61. Fox CH, Johnson FB, Whiting J, Roller PP. Formaldehyde fixation. The journal of histochemistry and cytochemistry : official journal of the Histochemistry Society. 1985; 33(8):845–853. [PubMed: 3894502]
62. Kucheryavykh LY, Kucheryavykh YV, Rolon-Reyes K, Skatchkov SN, Eaton MJ, Cubano LA, Inyushin M. Visualization of implanted GL261 glioma cells in living mouse brain slices using fluorescent 4-(4-(dimethylamino)-styryl)-N-methylpyridinium iodide (ASP+). BioTechniques. 2012; 53(5):305–309. [PubMed: 23570046]
63. Resende FF, Bai X, Del Bel EA, Kirchhoff F, Scheller A, Titze-de-Almeida R. Evaluation of TgH(CX3CR1-EGFP) mice implanted with mCherry-GL261 cells as an in vivo model for morphometrical analysis of glioma-microglia interaction. BMC cancer. 2015; 16(1):72. [PubMed: 26856327]
64. Zhang J, Kim S. Uncertainty in MR tracer kinetic parameters and water exchange rates estimated from T1-weighted dynamic contrast enhanced MRI. Magn Reson Med. 2014; 72(2):534–545. [PubMed: 24006341]
65. Nilsson M, van Westen D, Stahlberg F, Sundgren PC, Latt J. The role of tissue microstructure and water exchange in biophysical modelling of diffusion in white matter. Magma. 2013; 26(4):345–370. [PubMed: 23443883]
66. Szczepankiewicz F, Lasic S, van Westen D, Sundgren PC, Englund E, Westin CF, Stahlberg F, Latt J, Topgaard D, Nilsson M. Quantification of microscopic diffusion anisotropy disentangles effects of orientation dispersion from microstructure: applications in healthy volunteers and in brain tumors. NeuroImage. 2015; 104:241–252. [PubMed: 25284306]

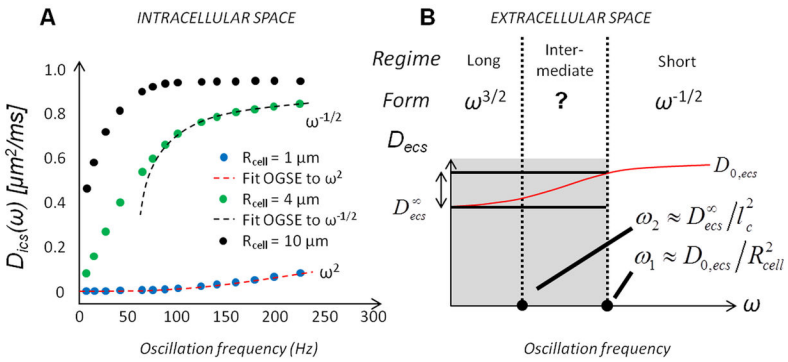

Figure 1.

Frequency-dependent diffusion inside (**A**) the intracellular space for various cell radii (numerical calcul, R_{cell} = 1/4/10 μm, blue/green/black circles) and (**B**) extracellular space in the long / intermediate / short time regime. **A.** Oscillation frequencies f_{OGSE} in the range [0–225] Hz are best suited to detect time-dependent changes from the intracellular compartment in cancer cells (R_{cell} = 4 μm). **B.** The analytical expression for diffusion in the ECS in the intermediate time domain is in general unknown (second column). Outside the short-time regime (i.e. within the grey area), small time-dependent variations are expected from the extracellular compartment (double arrow), compared to intracellular diffusivity changes inside cancer cells (Fig. 1A, green).

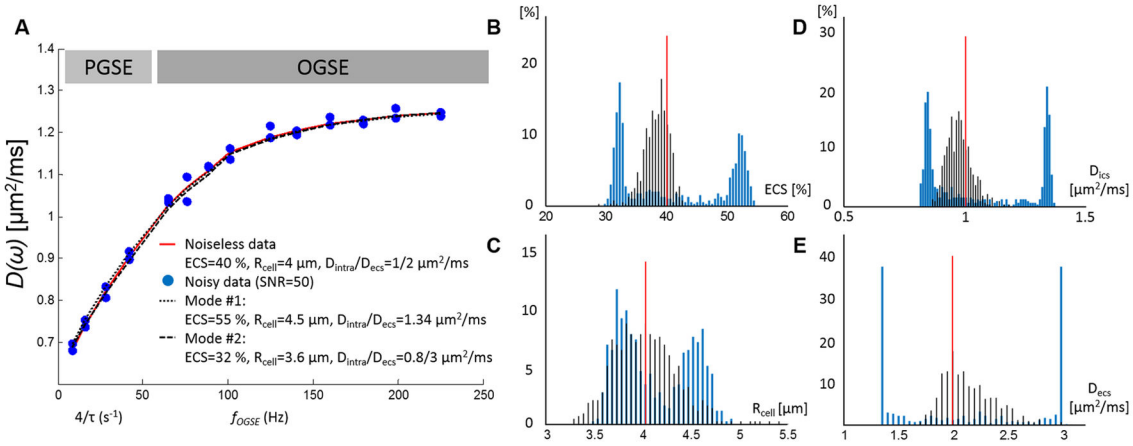

Figure 2.

Time-dependent diffusion over-fitting with four independent variables. **A.** Combination of PGSE and OGSE data (light and dark gray) in the range [31 ms ; 225 Hz] based on Eq. [3–6] and realistic estimates (ECS = 40%, R_{cell} = 4 μm, D_{ics}/D_{ecs}=1/2 μm^2/ms, $D_{0,ecs}$ = 2.7 μm^2/ms). When fitting four independent variables, small variations due to noise (blue circles, SNR=50, 2 time-points per time / frequency) lead to bimodal distributions (blue lines) of the estimated ECS fraction (B), cell radius (C), intra-(D) and extracellular diffusivities (E). The red lines correspond to the parameter nominal values. Alternatively, when D_{ics} is fully constrained based on Eq. [8a] and OGSE data in the short time regime (f_{OGSE} > 88 Hz), the distributions of the parameter estimates (black lines) are centered around the nominal values.

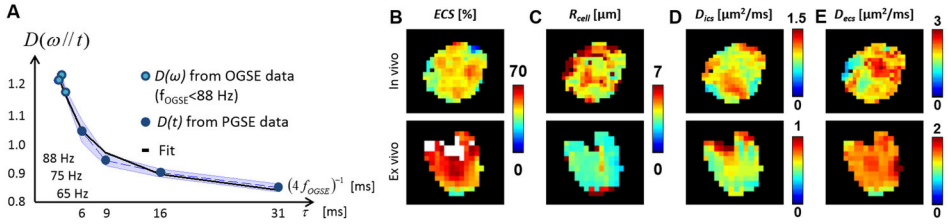

Figure 3. PGSE and low frequency OGSE time dependence

A. In the tumor, PGSE (open circles) and OGSE data (closed circles) are fitted to Eq. [8b] and [8c]. The standard deviation over the ROI is indicated by the blue area. Parametric maps of ECS (**B**), R_{cell} (**C**), D_{ics} (**D**) and D_{ecs} (**E**) inside the tumor in vivo / ex vivo (top / bottom line). White areas in ECS maps indicate regions of very low cellular density (ECS>70 %).

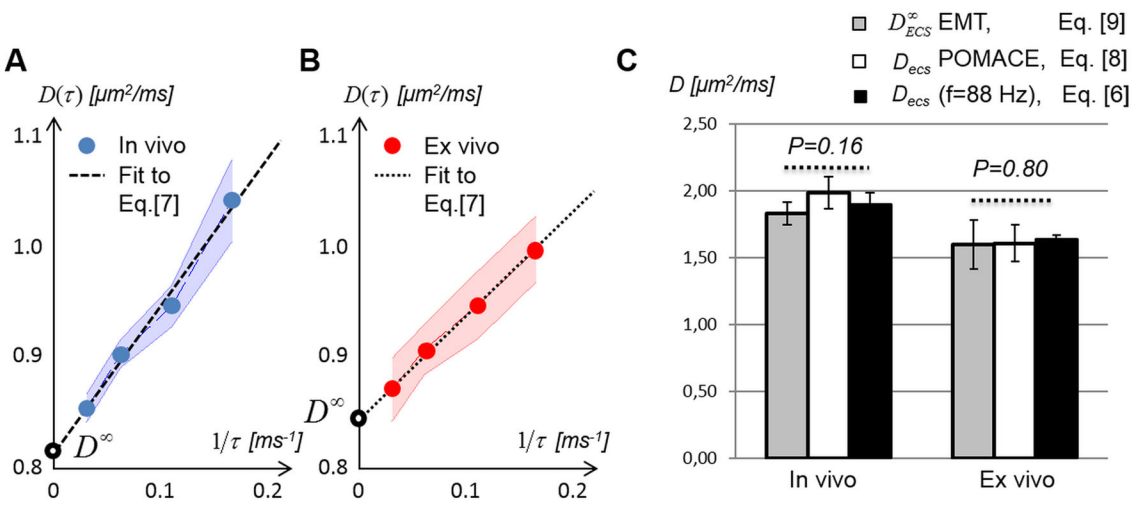

Figure 4. Long time-dependence of the diffusion coefficient in the tumor

Both **A.** in vivo and **B.** ex vivo PGSE-based $D(\tau)$ decrease linearly with $1/\tau$. Standard deviations within the tumor ROI are represented by the blue / red areas. **C.** Comparison of the ECS diffusivities derived from the POMACE model (D_{ecs}, white) with values extrapolated from the PGSE data in the long time regime (D_{ecs}^{∞}, grey), and from the short-time regime at f_{OGSE} = 88 Hz (black) for in vivo (left column) and ex vivo (right column) PGSE measurements.

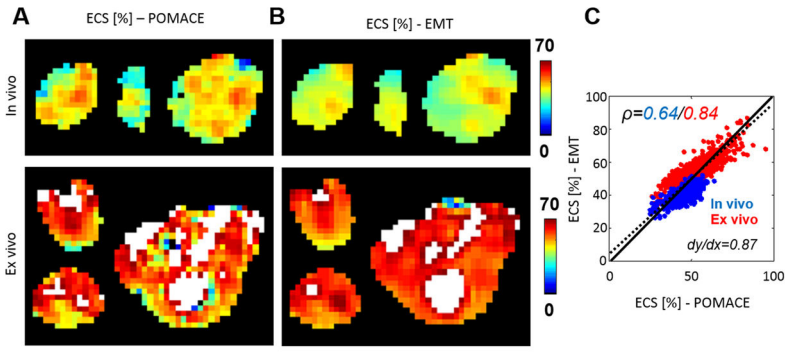

Figure 5. Comparison of ECS parametric maps

derived from **A.** the POMACE (Eqs. [8]) and **B.** EMT applied to the PGSE data (Eq. [9]) in three representative tumors. Areas of high *ECS* (>70%) are highlighted in white. **C.** At voxel level, *ECS* measurements appear strongly correlated in vivo (ρ =0.64) and ex vivo (ρ =0.84). The complete dataset (in vivo + ex vivo) is best fitted via the dotted line (slope=0.87). The unity line is plotted for visualization purposes.

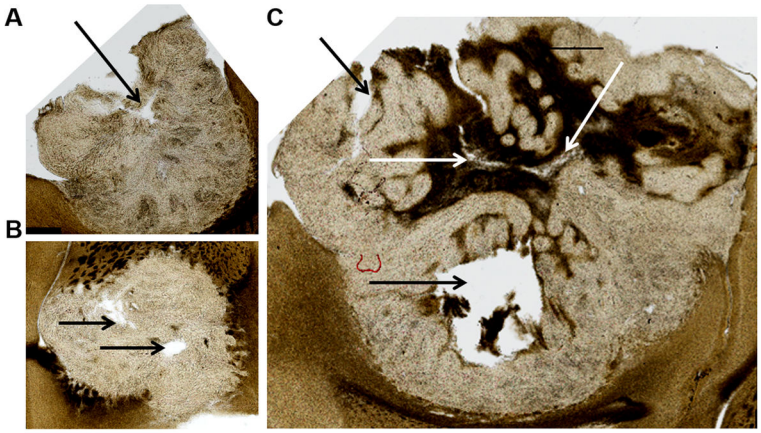

Figure 6. Optical microscopy

performed on brain sections (100 μm thickness) used for ex vivo MRI (corresponding to Fig. 5A–B, ex vivo panel). Necrotic areas (black/white arrows) match the regions of high *ECS* (>70 %) estimated using MRI (Fig. 5). Similarly, regions of low *ECS* appear to match areas of tumor infiltration in Gray and White Matter.

Table 1

In vivo (n=1056) and ex vivo (n=1073) fit estimates for the tumor environment. Only voxels with physically realistic values (D_{ecs} in [0–3] μm^2/ms, R_{cell} in [0–10] μm, ECS in [0–100] %) were included in this analysis.

	ECS [%]	R_{cell} [μm]	D_{ics} [μm^2/ms]	D_{ecs} [μm^2/ms]
In vivo	44 ± 7	4.8 ± 1.3	0.96 ± 0.21	2.06 ± 0.35
Ex vivo	54 ± 11	4.3 ± 1.4	0.76 ± 0.25	1.72 ± 0.25

Table 2

Pearson's correlation coefficients between *ECS*, R_{cell}, D_{ics}, D_{ecs} and diffusion coefficients obtained at two diffusion times (31/9 ms) and oscillation frequencies (65/225 Hz) derived in vivo (white) and ex vivo (gray).

Corr.	D_{PGSE} (31ms)		D_{PGSE} (9ms)		D_{OGSE} (65Hz)		D_{OGSE} (225Hz)	
ECS	**0.45**	**0.73**	**0.46**	**0.69**	0.22	0.41	0.29	0.51
R_{cell}	0.19	0.19	0.37	0.23	0.23	0.22	0.14	0.18
D_{ics}	0.21	0.25	0.40	0.36	**0.65**	**0.61**	**0.74**	**0.62**
D_{ecs}	0.19	0.13	0.08	0.15	0.30	0.31	0.13	0.21

Table 3

Comparison of *ECS* distributions for the two models. Only voxels with physically realistic values (D_{ecs} in [0–3] μm^2/ms, R_{cell} in [0–10] μm, *ECS* in [0–100] %) were included in this analysis.

ECS [%]	2CM - Eq. [8]	EMT, Eq. [9]
In vivo	44 ± 7	44 ± 5
Ex vivo	54 ± 11	56 ± 7